Journal of
Materials Chemistry A

RSCPublishing

PAPER

View Article Online
View Journal | View Issue

Cite this: *J. Mater. Chem. A*, 2013, **1**, 10193

Fundamental nature and CO oxidation activities of indium oxide nanostructures: 1D-wires, 2D-plates, and 3D-cubes and donuts†

Won Joo Kim,[a] Debabrata Pradhan[b] and Youngku Sohn*[a]

Various indium oxide nanostructures of 1D-wires, 2D-hexagonal plates, 3D-cubes and donuts were synthesized, and their fundamental characteristics and CO oxidation activities were studied in detail. X-ray diffraction and Raman analysis revealed that the as-synthesized wires and cubes are orthorhombic InOOH and cubic $In(OH)_3$, respectively. Upon annealing at 700 °C in air, all the as-prepared samples were recrystallized to cubic In_2O_3. The direct band gap of various as-synthesized nanostructures was estimated to be $\sim$2.7 eV from the UV-Vis absorption. Two broad photoluminescence peaks were found at 360 and 450 nm, which are attributed to the oxygen vacancies. The CO oxidation activities were in the order of hexagonal plates $\leq$ donuts < cubes < wires, tested by temperature-programmed reaction mass spectrometry. The difference in activity is explained on the basis of the surface area and oxygen vacancies of different nanostructures. In particular, the wires showed the CO oxidation onset at around 320 °C, which is 280 °C lower than that of hexagonal plates. The detailed morphology dependent properties and CO oxidation activities of various In_2O_3 nanostructures presented in this study provide new insights into sensor, energy, and environmental applications.

Received 14th June 2013
Accepted 24th June 2013

DOI: 10.1039/c3ta12312j

www.rsc.org/MaterialsA

Introduction

Semiconducting indium oxide (In_2O_3) has actively been studied fundamentally and technologically for wide applications in sensors, electronics/displays, catalysts, and solar cells.[1–5] Various synthetic (wet chemical and dry physical) methods have been employed to obtain diverse morphologies including cubes, rods, wires, belts, pyramids, tubes, hollow spheres, and flowers.[6–27] Zai *et al.* synthesized hierarchical In_2O_3 nanospheres and nanocubes by a ligand-assisted hydrothermal method, and reported BET surface areas of 38.15 and 13.97 $m^2\ g^{-1}$, respectively.[6] Hydrothermal and solvothermal methods have commonly been used for conveniently synthesizing In_2O_3 cubes and rods.[6–12] Yin *et al.* prepared uniform $In(OH)_3$ nanorod bundles with 200 nm thick and 3 μm long using ethylene glycol (EG) and ethylenediamine at 180 °C.[11] They obtained In_2O_3 upon annealing at 640 °C with no severe change in morphology. Ultrathin nanowires, nanobelts, and arrow-like nanostructures have generally been obtained by employing physical vapor deposition methods, and more easily than by wet chemical methods.[13–16] Maestre *et al.* synthesized arrow like nanostructures by the evaporation–deposition method.[13] Datta *et al.* obtained In_2O_3 bipyramids by a thermal conversion from In_2S_3 micropompons under oxygen conditions at 600 °C.[19]

In_2O_3 nanostructures with different morphologies (nanocubes, nanorods, hollow spheres, nanoparticles, nanobelts and mesoporous structures) have been prepared by the wet-chemistry route and applied for sensing gases such as H_2S, alcohols, CO, methane, and acetone.[17,28–32] In_2O_3 also has a high potential applicability as a catalyst in the steam reformation and photocatalytic dye degradation.[4,33–35] Bielz *et al.* demonstrated methanol steam reforming reaction, and explained high CO_2 selectivity to In_2O_3.[4] Yin *et al.* synthesized hollow rhombohedral In_2O_3 nanocrystals, and showed that it has 7–12 times superior photodegradation ability of rhodamine B and methylene blue, compared with those of commercial In_2O_3.[33] Segawa *et al.* used In_2O_3 (50–100 nm) particles as a catalyst for the dehydration of terminal diols and the reaction of monoalcohols.[34]

Motivated by high potential applicabilities of In_2O_3, we prepared various nanostructures, and investigated their fundamental nature. Since several studies have been reported on the gas sensing performance of In_2O_3, we focused on the less studied CO oxidation catalytic activity of the In_2O_3 nanostructures and demonstrate morphology dependent catalytic activity. In addition, the current studies report several new findings and advantages of In_2O_3. First, the catalytic properties could be used to predict relative gas (*e.g.* CO and O_2) sensing performance of In_2O_3 nanostructures because the adsorption of CO and O_2 is a common step for both sensing (of CO and O_2) and catalytic

---

[a] *Department of Chemistry, Yeungnam University, Gyeongsan 712-749, Republic of Korea. E-mail: youngkusohn@ynu.ac.kr; Fax: +82-53-810-4613; Tel: +82-53-810-2354*

[b] *Materials Science Centre, Indian Institute of Technology, Kharagpur 721 302, W.B., India*

† Electronic supplementary information (ESI) available. See DOI: 10.1039/c3ta12312j

reactions. Second, electronic wastes containing indium could be recycled as a catalyst. Third, this study revealed an unknown property (*e.g.* CO oxidation activity) of In_2O_3 and provides new basic scientific information which is useful for a clear understanding of the mechanism responsible for sensing and catalytic reactions, and development of efficient In oxide materials. In the present study, In_2O_3 wires are shown to have a lower temperature of CO oxidation activity than that of CeO_2 nanopowders, which have been widely studied as a CO oxidation catalyst support. This indicates that In oxide has potential for application as a catalyst.

Experimental section

For the synthesis of In_2O_3 nanostructures, we used water (or EG) as a solvent, and ethylamine (or ammonia and 0.1 M NaOH) to obtain precipitates. Briefly, 5.0 mL of 0.1 M indium sulfate solution was added into 15.0 mL of water (or EG) solvent, followed by ethylamine (or ammonia and 0.1 M NaOH). The solution was transferred into a 100 mL Teflon-lined stainless steel autoclave, and placed in a 120 °C (or 200 °C) oven for 12 h (or 72 h). The final products were fully washed with ethanol and Millipore water, and dried at 80 °C in an oven for further characterization. The surface morphology was examined by scanning electron microscopy (SEM, Hitachi SE-4800). For the transmission electron microscopic (TEM) and high resolution TEM studies, various In_2O_3 nanostructures were placed on carbon-coated Cu grids. The microstructures and electron diffraction patterns were taken using an FEI Tecnai G2 F20 TEM operated at 200.0 kV. X-ray diffraction (XRD) patterns were obtained using a PANalytical X'Pert Pro MPD diffractometer with Cu Kα radiation (40 kV and 30 mA). Thermogravimetric analysis (TGA) and differential scanning calorimetry (DSC) were performed using a TA Instruments thermal analyzer at a heating rate of 10 °C min^{-1}. UV-Vis absorption spectra were obtained using a Varian Cary 5000 UV-Vis-NIR spectrophotometer. A Bruker Senterra Raman spectrometer was employed to take Raman spectra of the samples, at a laser excitation energy of 532 nm. The Fourier transform infrared (FTIR) spectra were recorded using a Thermo scientific Nicolet iS10 spectrometer. Photoluminescence spectra were taken using a SCINCO FluoroMate FS-2. For 700 °C annealed samples, temperature programmed reduction (TPR) experiments were carried out using a Quantachrome ChemBET TPR/TPD apparatus under 5% H_2/Ar flow, at a temperature ramp rate of 10 °C min^{-1}. Before TPR, the sample was degassed at 200 °C under N_2 flow for 2 h. CO oxidation activities were tested at a heating rate of 20 °C min^{-1} under the flow of mixed CO (1%) and O_2 (2.5%) in N_2 using an SRS RGA200 quadrupole mass spectrometer. We used approximately 15 mg of a catalyst in a quartz U-tube (with an inner diameter of 4 mm). X-ray photoelectron spectroscopy (XPS) measurements were performed using a Thermo-VG Scientific MultiLab 2000 with a monochromatic Al Kα X-ray source (1486.6 eV) and a hemispherical energy analyzer.

Results and discussion

Fig. 1 shows the SEM images of as-prepared samples with various nanostructures before the thermal treatment. Fig. 1A shows the SEM image of the sample prepared in EG with ethylamine (EA) at 120 °C for 12 h. The morphology appears as nanorods with 100 nm long and <10 nm thick. The length and the width became longer and wider upon reaction for 72 h (Fig. 1A1), and at a higher temperature of 200 °C (Fig. 1A2), respectively. Yin *et al.* reported nanorods of 200 nm thick and 3 μm long using EG and ethylenediamine at 180 °C. Yang *et al.* synthesized nanorod bundles with 500 nm long and 200 nm thick.[12] Compared with the literature,[11,12] *we obtained much smaller nanorods*. When we used ammonia instead of EA, nanoparticles were obtained (ESI, Fig. S1†), consistent with the result reported by Yin *et al.*[11] With water as the solvent instead of EG, nanocubes were obtained with less than 50 nm width as shown in Fig. 1B. The size became smaller (less than 10 nm) upon adding less EA (Fig. 1B1). The temperature was not a major factor for controlling the size; no critical difference in size between 1B (200 °C for 12 h) and 1B2 (120 °C for 12 h) was observed. Fig. 1C and D show the SEM images of *donuts and hexagonal shaped crystals, which have never been reported before*. These shapes were found to be highly reproducible (ESI, Fig. S2†). With 1.0 mL of 1.0 M NaOH mixed in a 20.0 mL solvent (5.0 mL of water and 15 mL of EG), we obtained donut shape crystals of about 600 nm diameter at 120 °C for 12 h (Fig. 1C). At a higher temperature (Fig. 1C1) and a longer reaction time (Fig. 1C2), the size became slightly larger. Fig. 1D represents the SEM image of a sample prepared with 2.0 mL of 1.0 M NaOH and the sample morphology appears as ultrathin hexagonal plates. The hexagonal plates are uniform in size and highly symmetric with one side length of about 150 nm. These plates became more symmetrical at a higher temperature and with a longer reaction time. Upon annealing the as-prepared samples, the morphology was found to be changed to nanoparticles (for wires), distorted cubes (for cubes), cookies (for donuts), and cookie crumbs (for plates), as shown in the ESI, Fig. S3.†

Fig. 2 displays the XRD patterns of as-prepared and annealed samples with various morphologies as shown in Fig. 1. For the wires (Fig. 1A), the diffraction features are broad, and in very good agreement with those of orthorhombic (*P*21*m*) InOOH (JCPDS 1-071-2277). For the nanocubes (Fig. 1B), the XRD features are sharper, and all in very good agreement with the patterns of cubic ($Im\bar{3}$, JCPDS 1-076-1464) $In(OH)_3$. The major crystal planes are assigned to the diffraction peaks. For donuts and hexagonal plates prepared with the same 0.1 M NaOH, but different amounts of EG, the XRD patterns are very similar, indicating the compound with the same crystal structure. Upon annealing at 700 °C, all the samples showed the same XRD patterns (or the same crystal structure) of cubic In_2O_3 although there is a slight change in peak position and peak width. The most intense peak at $2\theta = \sim 30.6°$ is assigned to the (222) plane. The oxidation states of as-prepared samples were reported to be changed by the following chemical reactions: $2InOOH \rightarrow In_2O_3 + H_2O$, and $2In(OH)_3 \rightarrow In_2O_3 + 3H_2O$.[9,21] Very interestingly, Xu and Wang synthesized ultrathin (~2 nm) InOOH nanowires using oleylamine and ethanol at 180 °C by a hydrothermal method. They found that the InOOH transformed into cubic In_2O_3 by annealing in air. However, by capping the wires with

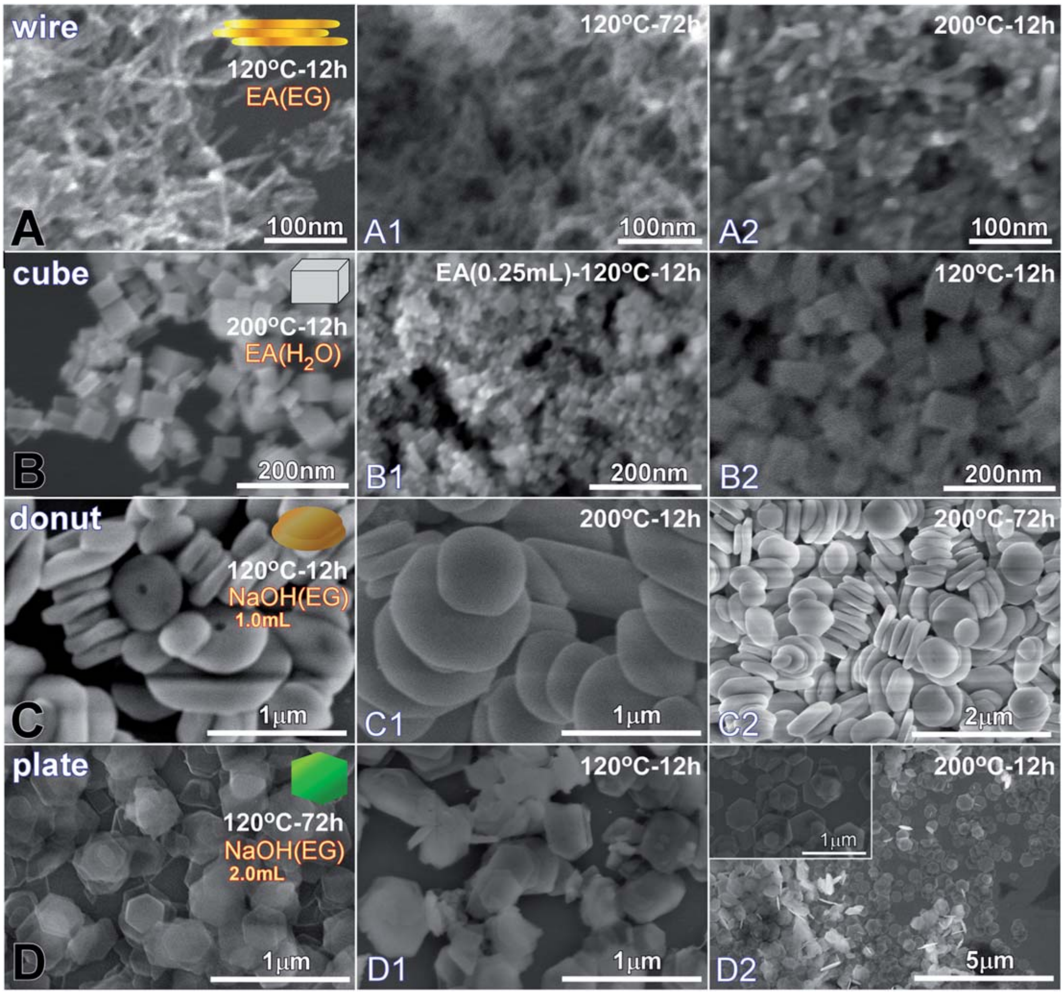

Fig. 1 SEM images of as-prepared indium nanostructures of wire, cube, donut, and plate shapes.

silica, the InOOH transformed into rhombohedral In_2O_3 by annealing at 400–700 °C. To compare with the literature results,[9] we also annealed the InOOH wires, and found that the wires transformed into rhombohedral In_2O_3 by annealing at 400 °C. Upon higher temperature annealing at 700 °C, the rhombohedral structure is further changed to a cubic crystal structure, as evidenced by the XRD analysis (ESI, Fig. S4†). Thermogravimetric and differential scanning calorimetry analysis (TG/DSC) curves for InOOH wires are provided in the ESI, Fig. S5,† confirming the compositional evolution from InOOH to In_2O_3.

On the basis of SEM and XRD results, we propose a growth mechanism of various nanostructures such as wires, cubes, donuts (ellipsoids) and plates. Fig. 3 shows the schematic representation of the formation of different nanostructures upon varying the morphology controlling reagents. The cubes with cubic $(lm\bar{3})$ $In(OH)_3$ crystal structure prepared by a hydrothermal method is known to have [111] as the preferential growth direction.[36–38] When ammonia (or an amine such as ethylamine) and water (or ethanol) were used in the synthesis, the surface energy of the {111} face is higher than others and therefore growth occurs on the same face. The other faces such as the oxygen-terminated {100} could be protected by RNH_3^+ ions,[39] which were formed by $RNH_2 + H_2O \rightarrow RNH_3^+ + OH^-$. As a consequence, the In^{3+} is hydrolyzed to form $In(OH)_3$ at the {111} face, leading to the formation of cubes. When the solvent was changed to EG, the In^{3+} of the {111} face could be capped by EG. This would lower the surface energy of the {111} face than that of the {100} face and therefore the [100] face becomes the preferential growth direction to form a wire structure.[9,38,40] Using NaOH instead of ethylamine, ellipsoid donuts and hexagonal plates were obtained. Here, NaOH plays an important role in capping the {001} faces. Therefore, with increasing $[NaOH]/[In^{3+}]$ mol ratio from 2.0 to 4.0, the ellipsoid structure changed to the hexagonal plate. The XRD patterns and the growth direction of the hexagonal plate are found not to match with the existing JCPDS data. Further investigation assisted by elemental analysis, XRD Rietveld analysis and high resolution TEM is underway to find the unknown crystal structure of donuts and hexagonal plates. Tentatively, we assume that at a lower concentration of NaOH, the surface capping by Na^+ is not efficient enough to form a plate structure. At a higher concentration of NaOH, the effect of capping by Na^+ becomes efficient to form hexagonal plates. This growth mechanism appears to be very similar to the [0001] growth direction of ZnO hexagonal

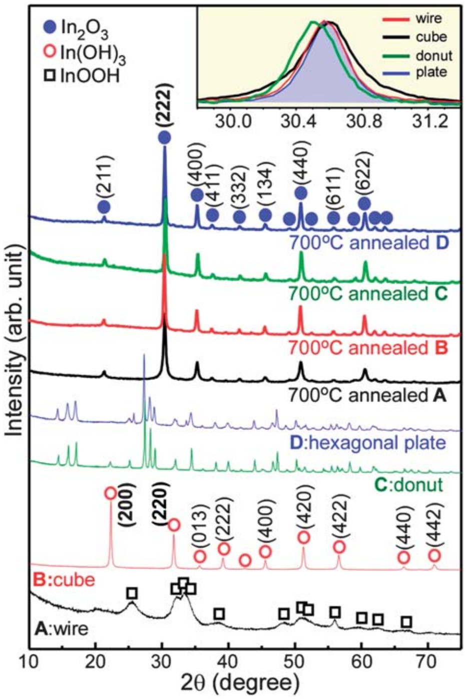

Fig. 2 Powder X-ray diffraction patterns of the as-prepared and 700 °C-annealed nanostructures. The inset shows the peaks of the (222) plane for 700 °C-annealed samples.

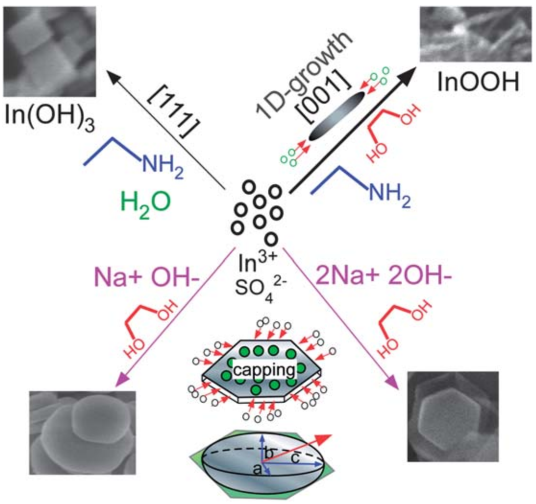

Fig. 3 The proposed crystal growth mechanism of wires, cubes, donuts and plates.

plates.[41,42] To check the role of alkali metals, we synthesized donuts and plates with 0.1 M LiOH and KOH solutions (1.0 mL). We obtained exactly the same crystal structures as those obtained with 0.1 M NaOH, but with a distortion of donut and plate shapes (not shown). However, when we used 2.0 mL of 0.1 M LiOH, no products were obtained. In addition, on the basis of our preliminarily XRD analysis for the fully washed donuts and plates, the SO_4^{2-} group should be included in the crystal structure. This group might be exposed to the terminated surface for Na^+ capping during the crystal growth.

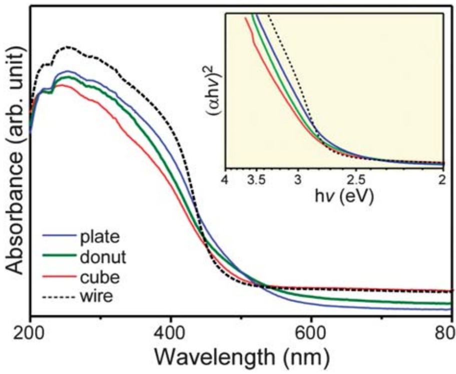

Fig. 4 UV-Visible diffuse reflectance absorption spectra of annealed indium oxide nanostructures (wires, cubes, donuts, and plates).

Fig. 4 displays the diffuse reflectance UV-Visible absorption spectra of annealed In_2O_3 samples. The absorbance (*Y*-axis) was converted from the diffuse reflectance by the Kubelka–Munk method. Inset plots of $[\alpha h\nu]^2$ *versus* $h\nu$ are used to determine the absorption edge (or the direct interband absorption gap) by the intersection of the two straight lines (from $[\alpha h\nu]^{1/2}$ and $h\nu$). The cross-absorption edges (or band gaps) for the In_2O_3 samples are very similarly located at around 2.7 eV. The actual direct band gap of In_2O_3 is somewhat controversial, reported between 2.3 and 3.8 eV.[43] Many studies have quoted ~3.75 eV for the direct band gap.[44,45] However, Walsh *et al.* predicted a much lower band gap, 2.9 eV, by first-principles calculations and X-ray spectroscopy.[46] Guo *et al.* synthesized In_2O_3 porous nanoplatelets, and measured a direct band gap of 3.1 eV.[5] Chen *et al.* reported a band gap of ~2.58 eV for In_2O_3 nanoparticles.[43]

Fig. 5 displays photoluminescence spectra of the as-prepared and 700 °C-annealed In_2O_3 samples. For the as-prepared samples, two broad peaks are commonly observed at 360 and 450 nm. Interestingly, the luminescence peak at 360 nm is dominant for wires, donuts, and plates, and the peak at 450 nm is minor. The relative luminescence intensities at 360 nm are different with morphology. However, for as-synthesized $In(OH)_3$ nanocubes, the luminescence at ~450 nm is stronger than the other at 360 nm. Upon annealing the samples, the photoluminescence spectra became very similar for all the samples with a decrease in the photoluminescence intensity. The two major peak positions at 360 and 450 nm show no critical change, but the ratio of their intensities *i.e.* I_{360nm}/I_{450nm} was reversed for wires, donuts, and plates. The luminescence peak of In_2O_3 at different wavelengths has commonly been attributed to different subgap (deep or shallow) energy levels of various oxygen defects (or vacancies), where the electron in the vacancy recombines with a hole to emit a photon.[11,22,47] The reported luminescence peak positions range from 340 nm to 640 nm, which depends on the preparation methods.[9,10,12,16,19,20,25,47–51]

Gan *et al.* employed an electrodeposition method to prepare In_2O_3 nanocubes deposited on a FTO glass, and observed a strong broad blue emission peak at 405 nm, attributed to singly ionized oxygen vacancies.[2] Chun *et al.* reported two broad peaks at 384 and 530 nm for In_2O_3 nanobelts prepared by chemical vapor deposition, attributed to near band gap emission and

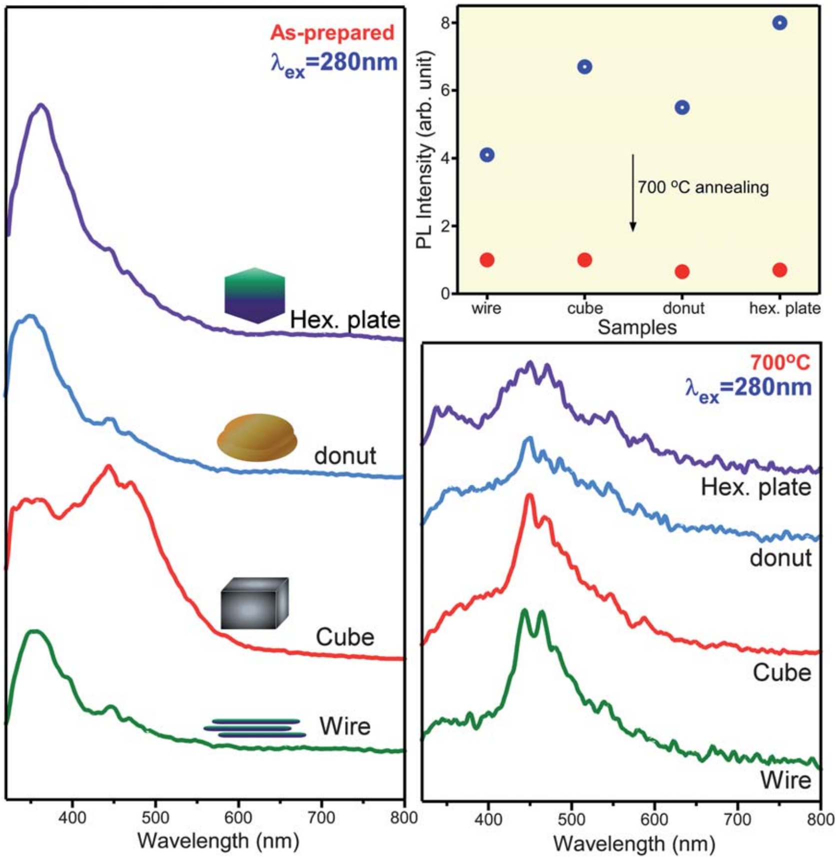

Fig. 5 Photoluminescence spectra of the as-prepared and 700 °C-annealed In_2O_3 samples at an excitation wavelength of 280 nm. The inset shows the relative PL intensities at ~360 nm and 450 nm emission peaks for the as-prepared and annealed samples, respectively.

oxygen vacancies, respectively.[16] On the basis of literature,[9,10,12,16,19,20,25,47–50] it can be concluded that the luminescence at longer (500–650 nm) wavelengths is due to deep oxygen vacancy energy levels of In_2O_3 samples prepared by a physical vapor deposition.[16,50] For the In_2O_3 prepared by a wet chemical method, photoluminescence appears between 400 and 500 nm, consistent with our results.[9,10,12,20,25,47–49]

Fig. 6 shows the Raman spectra of the as-prepared and annealed In_2O_3 samples. The corresponding FTIR spectra are provided in the ESI, Fig. S6.† For the as-prepared $In(OH)_3$ nanocubes, the Raman peaks are observed at 310 (In-O sym. stretching), 357 (In-O antisym. stretching), and 392 cm^{-1} (In-O antisym. stretching), consistent with the literature.[10,52] In the case of InOOH wires, Raman peaks are found at 195, 255, and 315 cm^{-1}, fairly consistent with the result by Yan *et al.*[53] For the annealed samples, we found Raman peaks at 132, 306, 365, 495 and 629 cm^{-1}, in agreement with the literature.[2,5,14,24,25,31] For the body-centered cubic In_2O_3, the vibrational modes are described as $4A_g$ (Raman active) + $4E_g$ (Raman active) + $14T_g$ (Raman active) + $5A_u$ (inactive for both Raman and IR) + $5E_u$ (inactive for Raman and IR) + $16T_u$ (IR active).[2,5,54,55] The width of E_g modes at 306 cm^{-1} show the order of wires < cubes < donuts ≈ plates, and the positions are slightly shifted to a lower wavenumber in the order of donuts ≈ plates < cubes < wire. For the annealed wires, the weak peak at 164 cm^{-1} is attributed to a vibrational mode of hexagonal In_2O_3.[56] For the annealed plates and donuts, we found an extra Raman peak at 464 cm^{-1}, although such differences were not found in the XRD patterns. This is tentatively attributed to a local structural defect.

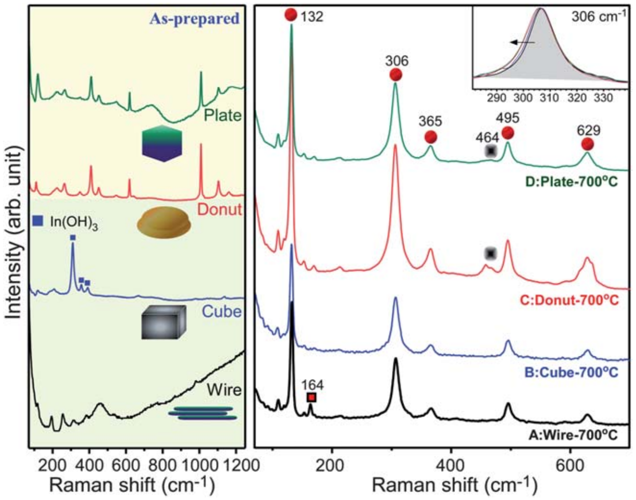

Fig. 6 Raman spectra of as-prepared (wires, cubes, donuts, and plates), and 700 °C-annealed In_2O_3 samples. The inset shows the normalized Raman peaks at 306 cm^{-1}.

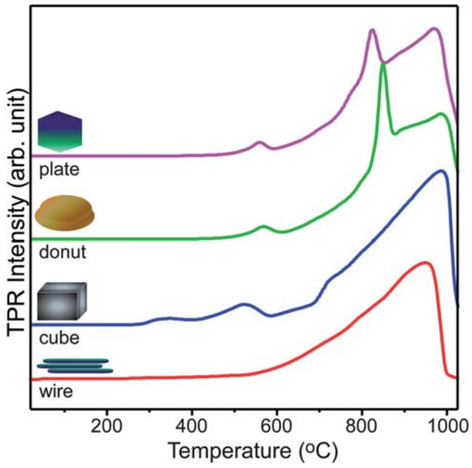

Fig. 7 Temperature-programmed H_2 reduction profiles of different shapes (wire, cube, plate, and donut shapes before annealing) of In_2O_3 samples.

Fig. 7 displays temperature-programmed H_2 reduction profiles for the four different In_2O_3 samples. A dominant peak is commonly found at 900 °C, which is attributed to the reduction of bulk In_2O_3.[34] The weak peak below 600 °C is likely due to the reduction of surface oxygen. The surface reduction peak positions are different with different samples; no peak for wires, 350 and 530 °C for cubes, and 570 °C for donuts and plates. Segawa *et al.* observed two broad reduction peaks at 200–400 °C (very weak) and 700 °C (strong), attributed to the reduction of surface oxygen and bulk In_2O_3, respectively.[34] These peaks are reported to be at a much lower temperature than those found in the present work. Interestingly, a sharp reduction peak is found at ~810 °C in the region of bulk reduction for donuts and plates. As mentioned in the Raman discussion (Fig. 6), this peak is likely due to the reduction at local sites in the In_2O_3 structure.

Fig. 8 shows the CO oxidation activities of the wires, cubes, donuts, and hexagonal plates. The CO oxidation reaction on an oxide catalyst strongly depends on the adsorption of CO and O_2 on its surface. In other expressions, the oxide surface is directly related to the sensing behavior of CO and O_2. For this reason, we could predict a relative gas sensing performance from the CO oxidation activity. In the 1st test run, the onset temperature of CO_2 formation is dramatically different for different samples. The wires and cubes show the onsets at 300 and 350 °C, respectively. The onset for donuts and plates is positioned at a much higher temperature of >850 °C. In addition to the CO_2 signal, we also detected the H_2O signal in the 1st test run by mass spectrometry. Since the as-prepared samples contain the –OH group, *i.e.* InOOH for wires and $In(OH)_3$ for cubes, H_2O evolution will occur *via* $2InOOH \rightarrow In_2O_3 + H_2O$, and $2In(OH)_3 \rightarrow In_2O_3 + 3H_2O$.[9,21,57] For the wires and cubes, the H_2O signal starts to appear at 200 °C, and the maximum peak intensity of H_2O is located at 380 °C. The H_2O signal is shaper and stronger

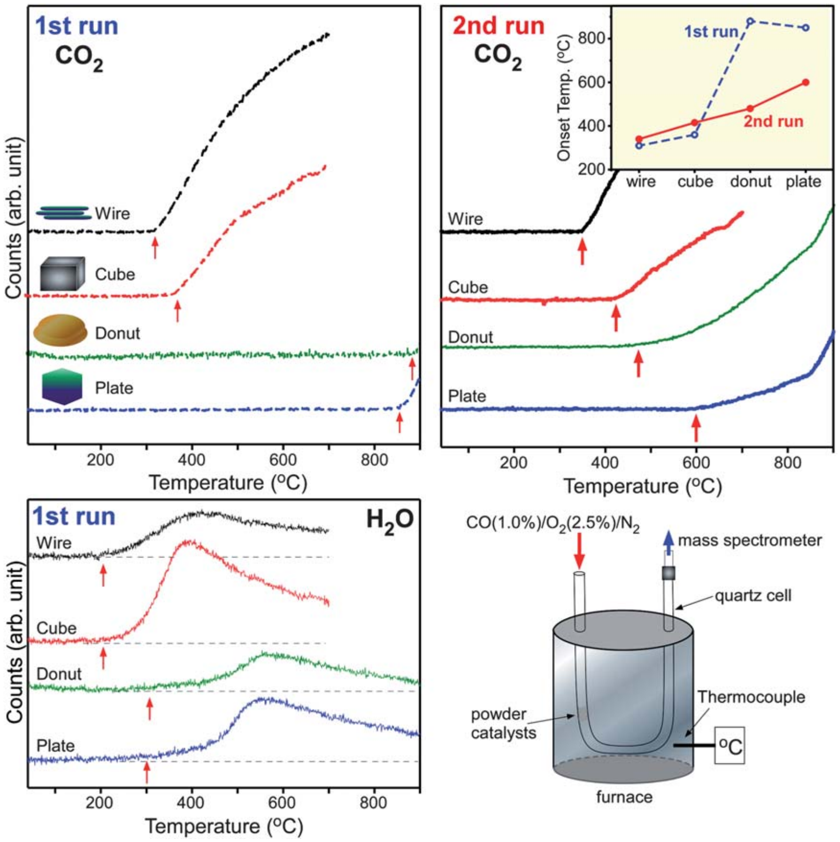

Fig. 8 The 1st and 2nd test runs of CO oxidation of different shapes (wire, cube, plate, and donut shapes before annealing) of as-prepared samples shown in Fig. 1. Schematics of the experimental setup for the CO oxidation test. The inset in the upper right displays the CO oxidation onset temperature.

for $In(OH)_3$ cubes than that for InOOH wires. On the basis of thermogravimetric and differential scanning calorimetric analysis for $In(OH)_3$,[9] an endothermic peak and weight loss occur at around 278 °C for $In(OH)_3$, consistent with our result. For InOOH, the thermogravimetric analysis curve is provided in the ESI, Fig. S5;† the weight gradually decreased from 100 to 550 °C.[21] In the 2nd test run, no H_2O signal was detected because of the complete conversion of In-OH to In-O structure in the 1st run. For the wires and cubes, the CO oxidation onset temperature was observed at a slightly higher temperature (or lower CO oxidation activity) by 15–35 °C. It appears that in the 1st run H_2O evolution plays a role in the CO oxidation activity which in turn depends on the morphology of sample. For the donuts and plates, the onset temperatures appear at much lower temperatures *i.e.* at 470 and 600 °C, respectively, compared with the 1st test run. However, compared with wires and cubes, the CO oxidation onset temperatures for the donuts and plates are located at higher temperature by 100–200 °C. In other words, the CO oxidation activity is poorer for the donuts and plates. It is worth comparing the CO oxidation activity of In_2O_3 with CeO_2 nanopowders (ESI†, Fig. S7), which is commonly used as a CO oxidation catalyst support. The CeO_2 nanoparticles with a diameter of about 20 nm were synthesized by a hydrothermal method at 120 °C for 12 hours. Very interestingly, the onset temperature of In_2O_3 (wire) was 50 °C lower than that of the CeO_2 nanopowders. This reflects that In_2O_3 shows a better catalytic performance, and has potential application in catalysis.[38,58]

To further explain the difference in CO oxidation activity, we examined BET surface areas of the annealed In_2O_3 samples and summarized them in Table 1. The BET surface areas of wires and cubes are 2–3 times larger than those of donuts and plates. The larger the surface area we expect the higher catalytic activity. Generally, the material with a high surface area shows higher gas sensitivity and catalytic activity. Interestingly, wires show higher catalytic activity by 50 °C even though its surface area is smaller than that of cubes, which indicates that the additional factors such as defects may play a role in the activity. As an additional factor, the oxygen vacancy is the most plausible. In the PL spectra (Fig. 5) discussed above, two broad peaks were attributed to two different oxygen vacancies, which may act as an active site for CO oxidation (or CO and O_2 adsorption). The ratio of $I_{360\mathrm{nm}}/I_{450\mathrm{nm}}$ was in the order of wires < cubes < donuts < plates, in good agreement with the order of the CO oxidation activity. The CO oxidation occurs by $CO + [M - O]^* \rightarrow CO_2 + M$, where $[M - O]^*$ is an active oxygen. The active oxygen site is most plausibly formed by chemisorption of molecular oxygen on oxygen vacancies. The different oxygen vacancies originate from the different recrystallization temperature forming cubic In_2O_3 in air (or oxygen) since all the as-prepared samples have different crystal structures. As discussed above, the wires with InOOH first change to rhombohedral In_2O_3 at 400 °C, and then to cubic In_2O_3 at 700 °C. The $In(OH)_3$ cubes and the donuts/plates convert to cubic In_2O_3 at above 400 °C and 700 °C, respectively. Intuitively, the different recrystallization temperatures result in different oxygen vacancies.

Table 1 BET surface areas ($m^2\ g^{-1}$) of various In_2O_3 nanostructures

Samples	Wires	Cubes	Donuts	Plates
Surface area ($m^2\ g^{-1}$)	16.1	19.0	6.8	5.9

XPS was employed to further understand the difference in CO oxidation activity and other related surface adsorption applications (*e.g.*, molecular sensing). Fig. 9 displays the survey and narrow scan (In 3d and O 1s) X-ray photoelectron spectra of various annealed In_2O_3 nanostructures. In typical survey scans before and after sputtering, indium, oxygen and carbon species were found as expected. For the narrow In 3d XPS spectra of the four different In_2O_3 samples before sputtering, In $3d_{5/2}$ and In $3d_{3/2}$ XPS peaks were commonly found at 444.8 (±0.1) eV and 452.4 (±0.1) eV, with a spin–orbit splitting of 7.6 eV, attributed to In of In_2O_3.[2,37,59,60] No critical difference in In 3d XPS binding

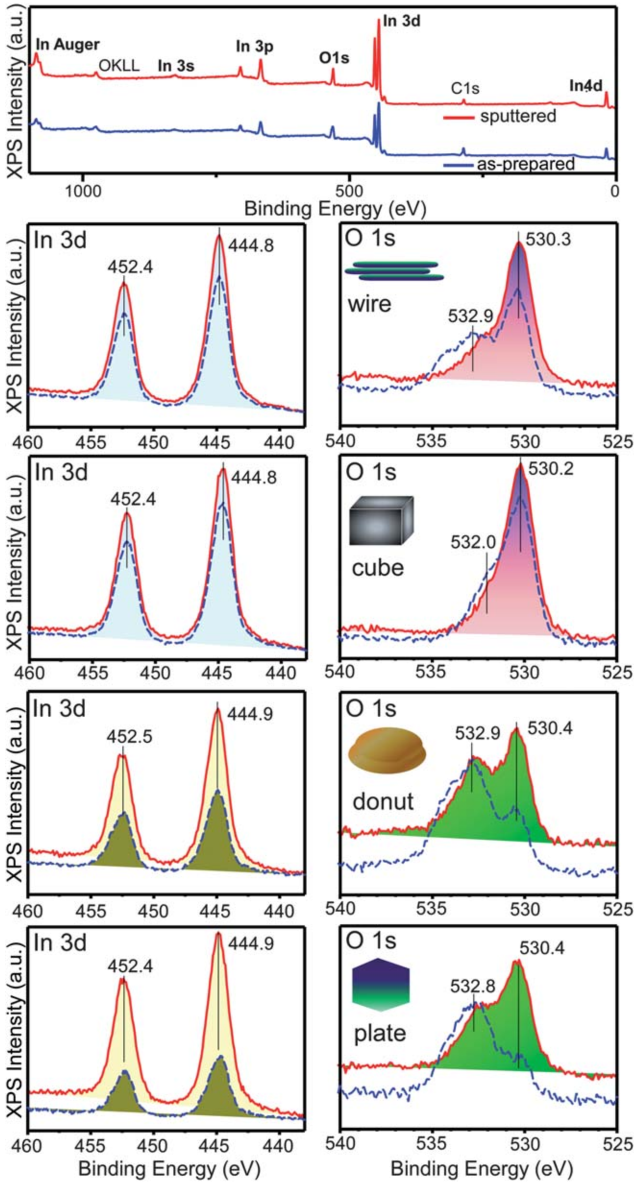

Fig. 9 Survey and narrow In 3d and O 1s XPS profiles of different shapes (wire, cube, plate, and donut shapes before annealing) of annealed In_2O_3 samples.

energy (BE) was found for the samples with different morphologies. However, upon sputtering the In_2O_3 samples the In 3d XPS showed a drastic change in the intensities. For the donuts and plates, the In 3d XPS peaks were more significantly increased upon removing adsorbed species by sputtering, compared with wires and cubes. For the O 1s XPS of wires and cubes, two broad peaks were commonly observed. The major peak at 530.3 (±0.1) eV was attributed to the lattice oxygen of In_2O_3.[2,37] The other (minor) higher BE peak could be due to adsorbed oxygen species such as OH and H_2O, which were substantially reduced upon sputtering. Interestingly, for donuts and plates before sputtering, the major peak was positioned at 532.9 eV, due to adsorbed oxygen species. The minor peak was at 530.4 eV, which became a major peak upon removing adsorbed species by sputtering. However, the higher BE peak still showed a significant intensity. As discussed above, the CO oxidation activity was lower for donuts and plates, compared with wires and cubes. This reflects that the oxygen sites play a major role in CO oxidation activity.

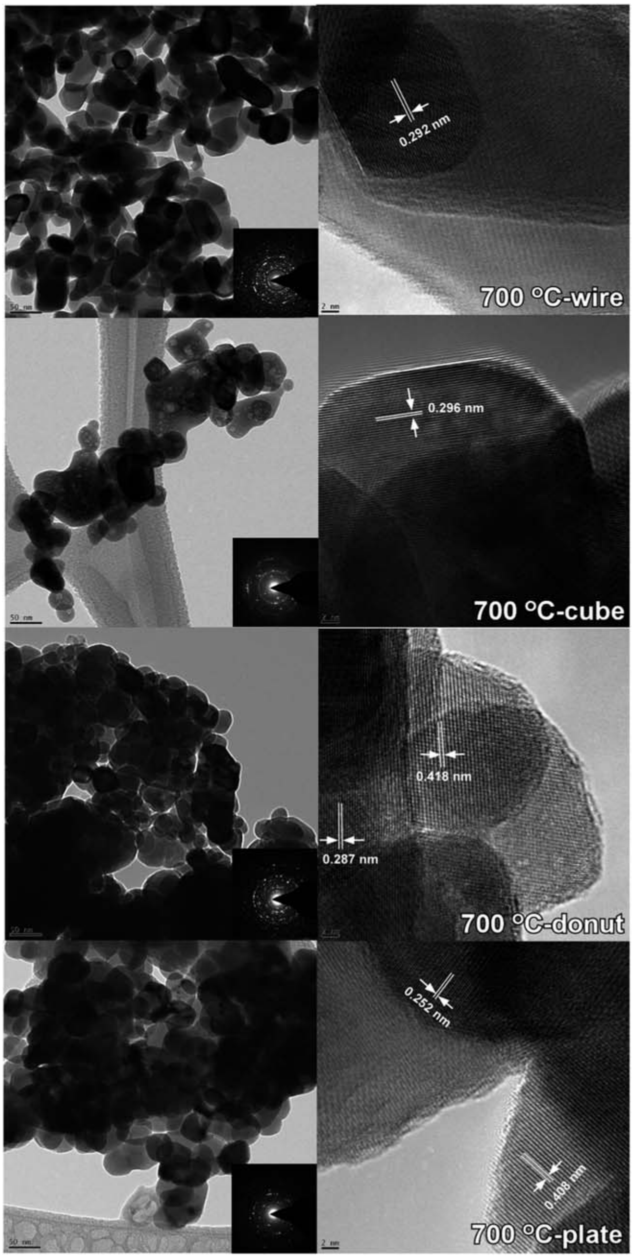

Fig. 10 TEM and HRTEM images of annealed wires, cubes, donuts, and plates. The inset shows the corresponding electron diffraction pattern.

Fig. 10 shows the TEM, HRTEM and electron diffraction patterns obtained for the four different In_2O_3 samples. On the basis of the TEM images, the donuts and plates appeared to be more aggregated, compared with the wires and cubes. As a consequence, the surface area is expected to be lower for donuts and plates, in good agreement with the experimental BET results (Table 1). For all the In_2O_3 samples, the electron diffraction patterns commonly showed the planes such as {222}, {400} and {440}, exactly as observed in the XRD patterns.[9,37,59,61] The HRTEM images of these nanostructures show the clear and continuous lattices indicating the crystalline nature of the materials, which correlates with the XRD results. A lattice spacing of ~0.29 nm (for wires and cubes), 0.41 nm (donuts), and 0.25 nm (plates) is measured from the HRTEM images.

Conclusions

We synthesized 1D-wires, 2D-hexagonal plates, 3D-cubes and donuts using ethylamine (and NaOH) in water (and ethylene glycol) solvent by a hydrothermal (and solvothermal) method. On the basis of XRD and Raman data, it was confirmed that the wires and cubes are orthorhombic InOOH and cubic $In(OH)_3$, respectively. All the 700 °C-annealed samples show cubic In_2O_3 with an estimated band gap of ~2.7 eV, lower than that mostly reported in the literature. Two broad photoluminescence peaks were found at 360 and 450 nm for the as-prepared and annealed samples attributed to the oxygen vacancies. The photoluminescence intensity ratio of I_{360nm}/I_{450nm} is greater than 1 for the as-prepared wires, donuts, and hexagonal plates, whereas about 1 for the as-prepared cubes. The photoluminescence profiles became very similar, and the I_{360nm}/I_{450nm} ratio is smaller than 1 upon annealing the as-prepared samples. The I_{360nm}/I_{450nm} ratio is the relative abundance of deep and shallow oxygen vacancies, and appears to be directly related to the relative CO oxidation activity. The morphology (*e.g.*, different surface area and oxygen vacancy) of samples is found to have a dramatic effect on the CO oxidation activities. The CO oxidation occurs by $CO + [M - O]^* \rightarrow CO_2 + M$, where $[M - O]^*$ is the active atomic oxygen in the lattice. The active oxygen appears to be directly related to the oxygen vacancies. The CO oxidation activities follow the order of hexagonal plates ≈ donuts ≪ cubes < wires in the 1st test run. During the 1st run, H_2O evolution also occurred accompanying a chemical reaction *i.e.* $2InOOH \rightarrow In_2O_3 + H_2O$, and $2In(OH)_3 \rightarrow In_2O_3 + 3H_2O$ for the as-synthesized InOOH and $In(OH)_3$ samples, respectively. The order of CO oxidation activity became plates ≪ donuts < cubes < wires in the 2nd test run. The wires showed the CO oxidation onset at around 320 °C, which is 280 °C lower (or more active) than that of hexagonal plates. The BET surface areas of annealed wires, cubes, donuts, and plates were measured to be 16.1, 19.0, 6.8, and 5.9 $m^2 g^{-1}$, respectively. The chemical states and local crystal structures of various In_2O_3 were further examined by X-ray photoelectron spectroscopy and HRTEM, respectively. Our findings on the morphology dependent material characteristics and catalytic activities provide new insights for developing indium oxide nanomaterials for sensor, energy, and clean environment applications.

Acknowledgements

This work was financially supported by the India-Korea joint project; the National Research Foundation of Korea (NRF) grant funded by the Korean government (MEST) (no 2012-0006296), and the Department of Science and Technology, New Delhi through the grant Indo-Korea/P-02.

References

1 M. G. Kim, M. G. Kanatzidis, A. Facchetti and T. J. Marks, *Nat. Mater.*, 2011, **10**, 382.
2 J. Gan, X. Lu, J. Wu, S. Xie, T. Zhai, M. Yu, Z. Zhang, Y. Mao, S. C. I. Wang, Y. Shen and Y. Tong, *Sci. Rep.*, 2013, **3**, 1021.
3 C. Li, D. Zhang, S. Han, X. Liu, T. Tang and C. Zhou, *Adv. Mater.*, 2003, **15**, 143.
4 T. Bielz, H. Lorenz, P. Amann, B. Klotzer and S. Penner, *J. Phys. Chem. C*, 2011, **115**, 6622.
5 L. Guo, X. Shen, G. Zhu and K. Chen, *Sens. Actuators, B*, 2011, **155**, 752.
6 J. Zai, J. Zhu, R. Qi and X. Qian, *J. Mater. Chem. A*, 2013, **1**, 735.
7 Q. Tang, W. Zhou, W. Zhang, S. Ou, K. Jiang, W. Yu and Y. Qian, *Cryst. Growth Des.*, 2005, **5**, 147.
8 J. Yang, C. Li, Z. Quan, D. Kong, X. Zhang, P. Yang and J. Lin, *Cryst. Growth Des.*, 2008, **8**, 695.
9 X. Xu and X. Wang, *Inorg. Chem.*, 2009, **48**, 3890.
10 F. V. Motta, R. C. Lima, A. P. A. Marques, M. S. Li, E. R. Leite, J. A. Varela and E. Longo, *J. Alloys Compd.*, 2010, **497**, L25.
11 W. Yin, J. Su, M. Cao, C. Ni, C. Hu and B. Wei, *J. Phys. Chem. C*, 2010, **114**, 65.
12 J. Yang, C. Lin, Z. Wang and J. Lin, *Inorg. Chem.*, 2006, **45**, 8973.
13 D. Maestre, D. Haussler, A. Cremades, W. Jager and J. Piqueras, *Cryst. Growth Des.*, 2011, **11**, 1117.
14 H. Dong, H. Yang, W. Yang, W. Yin and D. Chen, *Mater. Chem. Phys.*, 2008, **107**, 122.
15 G. Shen, B. Liang, X. Wang, H. Huang, D. Chen and Z. L. Wang, *ACS Nano*, 2011, **5**, 6148.
16 H. J. Chun, Y. S. Cho, i. S. Y. Bae and J. Park, *Appl. Phys. A: Mater. Sci. Process.*, 2005, **81**, 539.
17 Y. Li, J. Xu, J. Chao, D. Chen, S. Ouyang, J. Ye and G. Shen, *J. Mater. Chem.*, 2011, **21**, 12852.
18 P. Guha, S. Kar and S. Chaudhuri, *Appl. Phys. Lett.*, 2004, **85**, 3851.
19 A. Datta, S. K. Panda, D. Ganguli, P. Mishra and S. Chaudhuri, *Cryst. Growth Des.*, 2007, **7**, 163.
20 X. Tao, L. Sun, Z. Li and Y. Zhao, *Nanoscale Res. Lett.*, 2010, **5**, 383.
21 C. Chen, D. Chen, X. Jiao and C. Wang, *Chem. Commun.*, 2006, 4632.
22 C. Liang, G. Meng, Y. Lei, F. Phillipp and L. Zhang, *Adv. Mater.*, 2001, **13**, 1330.
23 M. Epifani, P. Siciliano, A. Gurlo, N. Barsan and U. Weimar, *J. Am. Chem. Soc.*, 2004, **126**, 4078.
24 C. Wang, D. Chen, X. Jiao and C. Chen, *J. Phys. Chem. C*, 2007, **111**, 13398.
25 H. Zhu, X. Wang, F. Yang and X. Yang, *Cryst. Growth Des.*, 2008, **8**, 950.
26 A. Gurlo, *Angew. Chem., Int. Ed.*, 2010, **49**, 5610.
27 C. H. Ho, C. H. Chan, L. C. Tien and Y. S. Huang, *J. Phys. Chem. C*, 2011, **115**, 25088.
28 D. Caruntu, K. Yao, Z. Zhang, T. Austin, W. Zhou and C. J. O'Connor, *J. Phys. Chem. C*, 2010, **114**, 4875.
29 D. Chu, Y. Zeng, D. Jiang and J. Xu, *Nanotechnology*, 2007, **18**, 435605.
30 W. J. Tseng, T. T. Tseng, H. M. Wu, Y. C. Her and T. J. Yang, *J. Am. Ceram. Soc.*, 2013, **96**, 719.
31 S. Elouali, L. G. Bloor, R. Binions, I. P. Parkin, C. J. Carmalt and J. A. Darr, *Langmuir*, 2012, **28**, 1879.
32 T. Waitz, T. Wagner, T. Sauerwald, C. D. Kohl and M. Tiemann, *Adv. Funct. Mater.*, 2009, **19**, 653.
33 J. Yin and H. Cao, *Inorg. Chem.*, 2012, **51**, 6529.
34 M. Segawa, S. Sato, M. Kobune, T. Sodesawa, T. Kojima, S. Nishiyama and N. Ishizawa, *J. Mol. Catal. A: Chem.*, 2009, **310**, 166.
35 H. Zhao, H. Dong, L. Zhang, X. Wang and H. Yang, *Mater. Chem. Phys.*, 2011, **130**, 921.
36 H. Zhu, K. Yao, Y. Wo, N. Wang and L. Wang, *Semicond. Sci. Technol.*, 2004, **19**, 1020.
37 C.-C. Huang and C.-S. Yehj, *Mater. Sci. Technol.*, 2004, **24**, 667.
38 L.-Y. Chen, Z.-X. Wang and Z.-D. Zhang, *New J. Chem.*, 2009, **33**, 1109.
39 K. H. L. Zhang, A. Walsh, C. R. A. Catlow, V. K. Lazarov and R. G. Egdell, *Nano Lett.*, 2010, **10**, 3740–3746.
40 Y. Fan, Z. Li, L. Wang and J. Zhan, *Nanotechnology*, 2009, **20**, 285501.
41 B. Panigrahy, M. Aslam, D. S. Misra and D. Bahadur, *CrystEngComm*, 2009, **11**, 1920.
42 J. Liu, L. Xu, B. Wei, W. Lv, H. Gao and X. Zhang, *CrystEngComm*, 2011, **13**, 1283.
43 S. F. Chen, X. L. Yu, H. Y. Zhang and W. Liu, *J. Hazard. Mater.*, 2010, **180**, 735.
44 A. K. Bal, A. Singh and R. K. Bedi, *Physica B*, 2010, **405**, 3124.
45 K. H. L. Zhang, A. Bourlange, R. G. Egdell, S. P. Collins, R. J. Bean, I. K. Robinson and R. A. Cowley, *ACS Nano*, 2012, **6**, 6717.
46 A. Walsh, J. L. F. Da Silva, S. H. Wei, C. Korber, A. Klein, L. F. J. Piper, A. DeMasi, K. E. Smith, G. Panaccione, P. Torelli, D. J. Payne, A. Bourlange and R. G. Egdell, *Phys. Rev. Lett.*, 2008, **100**, 167402.
47 Q. Tang, W. Zhou, W. Zhang, S. Ou, K. Jiang, W. Yu and Y. Qian, *Cryst. Growth Des.*, 2005, **5**, 147.
48 Z. Shi, W. Wang and Z. K. Zhang, *Mater. Lett.*, 2008, **62**, 4293.
49 T. J. Yan, X. X. Wang, J. L. Long, P. Liu, X. L. Fu, G. Y. Zhang and X. Fu, *J. Colloid Interface Sci.*, 2008, **325**, 425.
50 Y. Huang, K. Yu and Z. Zhu, *Cryst. Res. Technol.*, 2011, **46**, 90.

51 H. Zhou, W. Cai and L. Zhang, *Appl. Phys. Lett.*, 1999, **75**, 495.

52 A. Gurlo, D. Dzivenko, M. Andrade, R. Riedel, S. Lauterbach and H. J. Kleebe, *J. Am. Chem. Soc.*, 2010, **132**, 12674.

53 T. Yan, X. Wang, J. Long, H. Lin, R. Yuan, W. Dai, Z. Li and X. Fu, *New J. Chem.*, 2008, **32**, 1843.

54 C. Y. Wang, Y. Dai, J. Pezoldt, B. Lu, Th. Kups, V. Cimalla and O. Ambacher, *Cryst. Growth Des.*, 2008, **8**, 1257.

55 O. M. Berengue, A. D. Rodrigues, C. J. Dalmaschio, A. J. C. Lanfredi, E. R. Leite and A. J. Chiquito, *J. Phys. D: Appl. Phys.*, 2010, **43**, 45401.

56 D. Yu, S. H. Yu, S. Zhang, J. Zuo, D. Wang and Y. T. Qian, *Adv. Funct. Mater.*, 2003, **13**, 497.

57 X. Liu, L. Zhou, R. Yi, N. Zhang, R. Shi, G. Gao and G. Qiu, *J. Phys. Chem. C*, 2008, **112**, 18426.

58 B. Li, Y. Xie, M. Jing, G. Rong, Y. Tang and G. Zhang, *Langmuir*, 2006, **22**, 9380–9385.

59 L. Gai, L. Ma, H. Jiang, Y. Ma, Y. Tian and H. Liu, *CrystEngComm*, 2012, **14**, 7479.

60 J. Q. Xu, Y. P. Chen, Q. Y. Pan, Q. Xiang, Z. X. Cheng and X. W. Dong, *Nanotechnology*, 2007, **18**, 115615.

61 D. Chu, Y. Masuda, T. Ohji and K. Kato, *Langmuir*, 2010, **26**, 14814.